Experimental study on soil response and wave attenuation in a silt bed

Linlong Tong[a,b], Jisheng Zhang[a,b,*], Ke Sun[b], Yakun Guo[b,c,*], Jinhai Zheng[a,b], Dong-Sheng Jeng[a,d]

[a] State Key Laboratory of Hydrology-Water Resources and Hydraulic Engineering, Hohai University, Nanjing 210098, China
[b] College of Harbor, Coastal and Offshore Engineering, Hohai University, Nanjing 210098, China
[c] School of Engineering, University of Bradford, Bradford, BD7 1DP, UK
[d] Griffith School of Engineering & Cities Research Centre, Griffith University Gold Coast Campus, Queensland 4222, Australia

***** Corresponding author: jszhang@hhu.edu.cn; Y.Guo16@bradford.ac.uk

Abstract

When ocean waves propagate over porous seabed, they cause variations of the pore pressure within seabed, leading to the possible wave attenuation and soil liquefaction. In order to advance and improve our understanding of the process of wave-induced seabed liquefaction and its impact on wave propagation, systematical experiments are carried out in a wave flume with a soil basin filled with silt. Both the pore pressures and water surface elevations are measured simultaneously, while the seabed liquefaction is videotaped using a high-speed camera. Laboratory measurements show that the pore pressure in surface layer mainly oscillates over time, while the wave period averaged pore pressure has little change. In the deep layer, however, the wave period averaged value of the pore pressure builds up dramatically. The results show that the wave height decreases rapidly along the direction of wave propagation when seabed liquefaction occurs. Such a wave attenuation is greatly enhanced when the liquefaction depth further increases. The experiments also demonstrate that the conditions (wave height and wave period) of incident waves have significant impacts on the wave-induced pore pressures, liquefaction depth and wave attenuation in a silt bed.

Keywords：Liquefaction; Wave Attenuation; Excess Pore Pressure; Silt bed; Water Waves

1. Introduction

When wave-induced pressure exerts on the surface of the highly saturated seabed, the pore pressure within the seabed will vary with time and the cyclic changing shear stress will occur due to wave loading. The emergence of the excess pore pressure results in an instant variation of effective stresses. Such effective stresses and their corresponding soil strength will decrease when the excess pore pressure increases. Under certain conditions, the effective stresses vanish and the soil behaviors as a viscous fluid, which has no resistance to any shear loading. This phenomenon is the so-called Liquefaction (Sassa and Sekiguchi, 2001). This situation is frequently encountered in the marine environment with potential serious catastrophic consequences. For example, liquefaction induced by the wave-seabed interactions may result in an incline of offshore oil platform and serious subsidence of breakwaters. This demonstrates that the wave-seabed interactions have considerable impacts on the foundation stability of offshore infrastructures.

As ocean waves propagate over a seabed, the soil deformation will dissipate part of wave energy. The displacement of soil particles in soil layer increases significantly once the soil is liquefied. As such, the specific Coulomb friction loss (Yamamoto and Takahashi, 1985) increases rapidly and the wave height attenuates accordingly. This phenomenon has been studied since 1958 (Goda, 1958; Mathew et al., 1995), demonstrating that it is important to consider the impacts of seabed liquefaction on accurate wave prediction.

Due to its practical importance and theoretical interest, the mechanism of wave-seabed interactions has been theoretically and numerically investigated in the past several decades. For example, various models considering the porous seabed as a

poro-elastic material were developed for this purpose (Biot, 1941; Yamamoto et al., 1978; Hsu and Jeng, 1994; Zhang et al., 2011, Zhang et al., 2012; Lin et al., 2016; Sui et al., 2016). Although the build-up of the pore pressure due to contractive soil behavior was out of the scope of the above models, these models provide reasonable results if the plastic deformation of seabed was negligible. These studies show that the excess pore pressure fluctuates around a constant value and the period-averaged excess pore pressure almost remains the same. Momentary liquefaction may occur under certain wave conditions when the amplitude of excess pore pressure exceeds the initial effective stress (Sumer and Fredsøe, 2002). However, for the cohesive seabed (such as, silt or clay) with low permeability (Tzang et al., 2009), the wave-induced plastic deformation cannot be neglected (Sekiguchi et al., 1995). In these situations, the seabed response becomes highly nonlinear and the residual pore pressure is generated. Meanwhile, the propagation velocity of the shear waves becomes comparable to that of the water wave. If the shear stress ratio is sufficiently large that the wave-induced residual pore pressure exceeds the initial vertical effective stress, the residual liquefaction will occur. On this occasion, the porous elasto-plastic theories considering the importance of contractive soil behavior under wave loading are needed (Sassa and Sekiguchi, 2001; Miyamoto et al., 2004; Jeng and Ou, 2010; Liao et al., 2015).

Laboratory experiment is another common approach to investigate the soil response to the wave action. The primary experimental studies mainly include the water flume experiments (Tzang and Ou, 2006; Sumer et al., 2010; Zhang et al., 2016) and cylinder experiments (Zen and Yamazaki, 1990; Liu et al., 2015), which generally focus on the seabed instability induced by liquefaction. However, it is worth of pointing out that the cylinder experiments only consider the excess pore pressure

induced by macroscopic compression, while the water flume experiments investigate the excess pore pressure evolution characteristics under both the compression and shearing actions. The exception is the study of Sekiguchi et al. (1995), in which a centrifugal wave tests have been used to investigate the excitation of the excess pore pressure within the seabed as well as the seabed liquefaction under wave action. In centrifuge experiments, because the centrifugal acceleration is much larger than the gravitational acceleration, it can correctly represent the stress level at the field tests in the small-scale centrifuge wave tests. Some other studies indicate that sediment transportation is closely related to the seabed liquefaction (Tzang et al., 2009; Jia et al., 2014). The suspended sediment concentration near the mud-line increases substantially once the soil liquefied. The soil will experience a compaction process after liquefaction and the residual pore pressure will dissipate gradually. As a result, ripples will be formed on the bed, when the compaction process is completed (Miyamoto et al., 2004; Sumer et al., 2006).

As to waves, when seabed is liquefied, the velocity field near water-soil interface changes (Tzang et al., 2011) in which the horizontal velocity component decreases while the vertical velocity component significantly increases almost synchronously during the build-up stage of pore pressure. In front of breakwater, seawalls, and large caisson structures, standing waves will occur and the possible liquefaction induced by these standing waves is particularly investigated by Sassa and Sekiguchi (1999) and Wang et al. (2014). Compared to progressive wave, standing wave induced liquefaction exhibits some different features. For example, the pore pressure builds up rapidly near the node and subsequently the pore water spreads out towards the antinodes (Kirca et al., 2013). In addition, standing wave has a significant impact on the stability of coastal and offshore structures.

Although a substantial amount of knowledge has been gained on wave-seabed interactions, majority of these studies only consider the changes of seabed, e.g. pore pressures, soil stresses or volume deformation. There is little study considering the wave evolution in the period of the excess pore pressure build-up to soil liquefaction. Mathew et al. (1995) found that the wave attenuation was correlated to fluid mud generated by mud banks liquefaction in their situ examination. Unfortunately, there was no information reported about the pore pressure evolution within the seabed during this process. Using physical experiments, de Wit and Kranenburg (1996) found that the turbulence intensities in the water layer decreased and wave decay was observed when waves propagated over a layer of fluid mud. However, there is no information about the pore pressure reported in their study.

The purpose of this study is therefore to investigate the response of silt bed to progressive waves and the corresponding wave attenuation using laboratory experiments. Both the pore pressure in the soil and the wave height are measured in the laboratory tests. The development process and features of the excess pore pressure in silt bed are analyzed. Significant attenuation of wave height has been observed once the seabed liquefied and it has close relationship with seabed response.

2. Experimental facilities, measurements and procedure

2.1 Wave flume and instrumentations

A water wave flume with a dimension of 48 m (length) × 0.5 m (width) × 1 m (height) is used for laboratory experiments. The flume is equipped with a piston-type wave maker and wave energy absorbing sloping beaches at two ends of the flume. As shown in Fig.1(*a*), a soil basin with a dimension of 5.3 m (length) × 0.5 m (width) ×

143 0.4 m (height) is formed by two artificial trapezoids (false floors) in the middle of
144 wave flume. The inclined plane of the trapezoid located near the wave maker forms a
145 gentle ramp with a slope of 1:10. The false floor and the gentle ramp provide smooth
146 transition for wave propagation. A ramp with a slope of 1:2.5 is inserted at the other
147 end of the trapezoid near the wave energy absorbing beach side.
148
149 The excess pore water pressure and water surface elevation are measured in the
150 experiments. The excess pore pressure induced by the waves is recorded by ten
151 miniature pore pressure transducers (PPTs) whose diameter is 6mm and is covered by
152 an argil filter (see Fig. 1(*b*)). In particular, one PPT is installed at the mud-line surface
153 to measure the pressure exerted on the bed surface and also serves as a reference
154 measurement. Six conventional capacitive wave gauges are utilized to measure the
155 water surface elevation and their locations are shown as in Fig. 1(*a*). The sampling
156 frequency of the wave gauges and pore pressure transducers is set to 50 Hz for all
157 experiments.
158
159 2.2 Soil parameters
160 The soil used in the experiments is a commercially available silica flour, which is silt
161 type (mainly mineral composition of silica, alumina) with a mean grain size d_{50}=0.042
162 mm. Physical properties of the silt are listed in Table 1, in which $e_{\max}$ and $e_{\min}$ are
163 the volume void ratio of the loosest and the densest state, respectively, and e is the
164 void ratio. The sample is taken from the point 20 cm below the mud-line in the middle
165 of basin after the experiment. D_r is the relative density defined as

166 $$D_r = \frac{e_{\max} - e}{e_{\max} - e_{\min}} \quad (1)$$

167 The soil porosity (n) is related to the void ratio as $n = e/(1+e)$. The submerged

specific gravity of the sample is given by $\gamma' = (1-n)(\gamma_s - \gamma_w)$, where γ_w and γ_s are the specific weight of water and soil grains, respectively. In saturated seabed it can be written as $\gamma' = \gamma_t - \gamma_w$, where γ_t denotes the total specific weight of soil calculated as $\gamma_t = (s+e)/(1+e)$ with *s* representing the ratio of the specific weight of soil grains to that of water.

2.3 Test conditions

The test conditions are summarized in Table 2. The water depth (*h*) of all tests is kept as constant of 35cm. In Table 2, *H* and *T* denote the wave height and wave period, respectively. U_m is the maximum value of the orbital velocity at the bed surface, and U_{fm} is the maximum value of the undisturbed friction velocity which is given by

$$U_{fm} = \sqrt{\frac{f_w}{2}} U_m \tag{2}$$

where f_w is wave friction coefficient given by $f_w = 2/\sqrt{R_e}$, and R_e is the Reynolds number defined as $R_e = (aU_m)/\nu$, where *a* is the amplitude of the orbital motion of water particles at the bed and can be calculated according to linear wave condition, ν is the kinematic viscosity of water. The Shields parameter θ is defined as

$$\theta = \frac{U_{fm}^2}{g(\rho_s/\rho_w - 1)d_{50}} \tag{3}$$

in which *g* is the acceleration due to gravity, ρ_s and ρ_w are the density of soil particle and water, respectively, d_{50} is the median particle size for which 50 percent of particles by weight are finer.

2.4 Test procedure

The procedure adopted in the experiments is summarized as follows:

(1) The flume including soil basin is emptied and cleaned, while the PPTs are placed under water for 24h and exhausted to guarantee the argil filter covers being free of air.

(2) The soil basin is filled with water and the PPTs are installed at the prescribed specific positions (see Fig. 1(*b*)).

(3) An electric handheld mixer is then used to thoroughly mix the soil and water into thick slurry in an iron container. The thick slurry is then uniformity injected into the soil basin to form a layer of the soil bed which is allowed to settle and consolidate for several hours. This process is repeated until the mud-line reaches the top rim of the trapezoids. The surface of the seabed is then leveled off smoothly.

(4) Water is slowly pumped into the flume until the designated depth is reached. The seabed is then allowed to have final settle and consolidation for several days.

(5) The wave height gauges are installed at the prescribed specific positions for the monitoring and measurement of water elevations.

(6) The experimental run starts by switching on the wave maker, PPTs and wave height gauges. The relevant experimental data are recorded, measured and collected accordingly for a certain period as required.

3. Liquefaction Criterion

When wave trains propagate over the silt bed, as shown in Fig. 2, they will generate the pore pressure, which varies from the hydrostatic value (u_{st}) to u. This generates the excess pore pressure, u-u_{st}, denoted as u_e. As suggested by Sassa and Sekiguchi (1999), the excess pore pressure u_e can be divided into two components, namely

$$u_e = u_e^{(1)} + u_e^{(2)} \tag{4}$$

where $u_e^{(1)}$ represents the oscillatory component whose temporal average over any

wave period is zero by definition; $u_e^{(2)}$ stands for the residual pore pressure, which essentially stems from cyclic plasticity (contractive behavior) of the soil and is calculated as:

$$u_e^{(2)} = \frac{1}{T}\int_{t-0.5T}^{t+0.5T} u_e dt \tag{5}$$

Previous experimental studies show that both $u_e^{(2)}$ and u_e has a peak value, denoted respectively as $u_{e,\max}^{(2)}$ and $u_{e,\max}$.

In previous experimental studies, when the residual pore pressure ($u_e^{(2)}$) exceeds the initial vertical effective stress, the soil is considered as liquefied (Foda and Tzang, 1994; Sassa and Sekiguchi, 1999). This is the state of soil skeleton eventual failure. The weight of soil particle is supported by the pore fluid. Following these studies, the excess pore pressure ($u_e^{(2)}$) is taken as the liquefaction discrimination index in this study, which can be expressed as

$$u_e^{(2)} + \gamma' z > 0 \tag{6}$$

where *z* indicates the vertical coordinate of a generic point, as defined in Figure 2.

4. Results and discussions

4.1 Observations

In the present study, the experimental tests including both liquefaction and non-liquefaction cases are videotaped by using a high-speed camera which is placed outside the flume. In Test 1 (non-liquefaction case), the visibility of water is generally good although a few soil particles are suspended by wave generated turbulence. It is found that the suspended sediment concentration is very low. Moreover, the suspended particles are mainly distributed near the bottom of water body. The silt bed

has little change over time. Figure 3(*a*) is a time series of video frames taken during this test. However, a different phenomenon is observed in the other tests when liquefaction occurs during the experiments as shown in Figure 3(*b*). In this situation, the suspended sediment concentration increases rapidly after several cycles of wave loading, resulting in a turbid water. An obvious back and forth motion of soil particles (acting as heavy fluid) is observed to appear at the surface layer of the silt bed. Due to poor visibility, the water-soil bed interface is indicated by using yellow dash lines in Figure 3(*b*). In order to clearly show the oscillation of liquefied soil, a time series of closely recorded video shots are shown in Figure 4 for Test 6. The figure shows that the oscillation amplitude of the liquefied soil is about 0.55 cm. It is seen that the sandy clouds (Tzang et al., 2009) rise from the silt bed surface. These sandy clouds are thought to be generated by the velocity shear stress at the seabed surface.

After the wave maker is switched off (i.e., the wave loading is stopped), the soil is consolidated under its self-gravity. This process takes a long time because the pore-water drains out slowly. Observations reveal that there are many tiny cracks distributed in the surface layer of silt bed during this period (see Fig. 5). These cracks are probably due to the relatively small consolidation stress and the weak resistance of soil skeleton at the silt bed surface, forming the seepage channel for pore water. This observed phenomenon differs from that observed by Sumer et al. (2006). In their experiments (d_{50}=0.060 mm), they observed the formation of ripples at the soil surface during the consolidation period. This discrepancy may be mainly ascribed to the fact that the finer soil particles are used in the present study.

4.2 Soil response

In the present experiments, two types of pore pressure response are found and

267 measured. The first one shown in Fig. 6(*b*) is similar to the dynamic water pressure
268 measured at the interface (see Fig. 6(*a*)), in which the horizontal axis is the number
269 of wave cycle, *N*. As shown in the figure, the residual component of pore pressure is
270 negligible and the oscillatory mechanism will dominate the whole process. This type
271 of pore pressure response is always found at the surface layer of the soil (e.g. in Point
272 2 and Point 3). This phenomenon is mainly due to two factors: (1) the pore water
273 drains out quickly as the soil is loose and the permeability is relatively high at the
274 surface layer; (2) the buried depth of the PPT at the surface layer changes with
275 elapsed experimental time due to the sediment transport and scour. On one hand, the
276 soil particles are affected by the wave induced oscillatory flow and partial soil
277 particles suspended. On the other hand, the liquefied soil layer oscillates over time
278 like the water wave as shown in Fig. 4 though the oscillation amplitude and period
279 differ from those of water wave. The wave and liquefied seabed may be simulated as a
280 two-layer flow system (Sassa and Sekiguchi, 1999)
281
282 The other type of pore pressure response is shown in Fig. 6(*c*), which indicates that
283 the residual component of the pore pressure significantly increases after several cycles
284 of wave loading due to the plastic deformation of the soil. It is seen that the amplitude
285 of oscillatory pore pressure increases quickly during the accumulation process of pore
286 pressure. This is because the elastic deformation of soil grows since the resistance of
287 soil decreases under the cyclic wave loading. As a result, the amplitude of oscillatory
288 pore pressure increases.
289
290 4.2.1 Comparison with numerical simulation
291 Some theoretical studies for the wave-induced pore pressure accumulation in marine
292 sediments have been carried out since 1978 (Seed and Rahman, 1978). Most previous

studies including analytical and numerical models have based on Seed and Rahman's (1978) model. In their approach, the source term, representing the pore pressure generation due to oscillatory shear stresses, was included in the conventional consolidation equation. The maximum oscillatory shear stress amplitude during the wave loading was used in their 1D model. Based on this 1D model, several analytical solutions were proposed (McDougal et al., 1989; Sumer and Fredsøe, 2002; Jeng and Seymour, 2007). Recently, Jeng and Zhao (2015) further extended this 1D Seed-Rahman model to 2D and introduced the new definition of source term in the governing equations by instant amplitude of oscillatory shear stresses.

In this section, we further compare our experimental results with Jeng and Zhao (2015) 2D numerical model. The results of both models with the maximum shear stress and instant shear stress under linear wave loading are included in Figure 7(*a*). As shown in the figure, the instant model provides a better prediction of residual pore pressure than the maximum model (at t=100 s). Figure 7(*b*) is the comparison between numerical simulation (solid lines; Jeng and Zhao, 2015) and the present experiments (symbols) for various wave heights. As shown in Figure 7(*b*), the numerical model (Jeng and Zhao, 2015) can only predict the pore pressure with reasonable accuracy for small wave height (i.e. Test 1), while large deviation exists between the numerical simulation and experimental measurements for large wave heights. Referring to Table 2, for the case presented in Figure 7(*a*), no liquefaction occurs in Test 1. For other three cases with larger wave heights, liquefaction occurs. This explains why the numerical model cannot provide a prediction with acceptable accuracy because it does not work for the case after liquefaction. To further investigate the process of post-liquefaction, the 1D progressive liquefaction model (Sassa and Sekiguchi 2001; Liu et al., 2008) needs to be further extended to 2D for other tests.

4.2.2 Effects of wave height

In order to investigate the effects of wave height on soil response in vertical direction, the tests with a wave period of 1 s are chosen for demonstration purpose. The maximum excess pore pressure at profile A-A is plotted in Fig. 8 in which the dash line represents the liquefaction line; while the dots indicate the measured maximum pore pressure. According to the liquefaction criterion described in Section 3, the wave height of 4 cm is the only no-liquefaction case as all $u_{e,\max}^{(2)}$ points are below the liquefaction line. This means that the maximum values of the residual pore pressure are smaller than the incipient vertical effective stress for liquefaction (e.g. $u_{e,\max}^{(2)} / \gamma' d = 0.31$ at d=2 cm, $u_{e,\max}^{(2)} / \gamma' d = 0.07$ at d=9 cm and $u_{e,\max}^{(2)} / \gamma' d = 0.014$ at d=27 cm). The soil liquefaction takes place for other cases and the liquefaction potential increases with the increase of wave height. This phenomenon can be explained as following from the point of view of soil dynamics.

Once the wave loading exerts on soil bed, it induces the volumetric strain, effective stresses and the pore pressure variation within soil bed. The effective stresses induced by waves can be divided into two parts:

$$\boldsymbol{\sigma} = p\boldsymbol{\delta} + \boldsymbol{s} \tag{7}$$

where $\boldsymbol{\sigma}$ is the total effective stresses, p represents the value of spherical stress, $\boldsymbol{\delta}$ is Kroenke symbol and $\boldsymbol{s}$ indicates the deviatory stress. The storage equation of the deformable soil with compressible pore water can be expressed as

$$\frac{\partial \varepsilon}{\partial t} - n\beta \frac{\partial u_e}{\partial t} = \nabla \cdot \boldsymbol{q} \tag{8}$$

where ε is the total volumetric strain due to wave loading, β is the coefficient of compressibility of the pore water, ∇ is the Hamilton operator, $\boldsymbol{q}$ represents the

discharge velocity of the pore water. According to the Darcy's law, the component of $\boldsymbol{q}$ can be given as

$$q_i = -k_s \frac{\partial}{\partial x_i}\left(\frac{u_e}{\gamma_w} + h + d\right) = -\frac{k_s}{\gamma_w}\frac{\partial u_e}{\partial x_i} \tag{9}$$

where k_s is the permeability of the seabed. The total volumetric strain of silt induced by cyclic wave loading also consists of two parts, an elastic component (ε_e) and a plastic component (ε_p):

$$\varepsilon = \varepsilon_e + \varepsilon_p \tag{10}$$

The elastic component (ε_e) is recoverable during each wave cycle which is mainly related to the spherical stress:

$$d\varepsilon_e = Kdp \tag{11}$$

where K is the bulk modulus of soil. The plastic component (ε_p) can be indicated by the cycle stress ratio. For a large wave height, the wave induces a great value of deviatory stress ($\boldsymbol{s}$) and cyclic stress ratio in the silt bed (Sassa and Sekiguchi, 1999). As the result, the maximum pore pressure grows and approaches to the liquefaction line. Consequently, the maximum liquefaction depth increases as the wave height increases.

4.2.3 Effects of wave period

In addition to wave height, wave period can also affect the soil response significantly. To evaluate the effect of the wave period on soil response, runs are conducted for otherwise the same conditions but with various wave periods. The experiments show that the liquefaction potential increases with the increase of wave period for the parameters investigated in this study. This is demonstrated in Test 1 in which soil is not liquefied for wave period of 1 s, but it is liquefied in Test 2 and Test 3 which have

368 the same wave height of *H*=4 cm but with longer wave period. The measured
369 maximum excess residual pore pressure of PPT 9 in Test 2 (*H*=4 cm, *T*=1.4 s) is 2.05
370 kPa, which is lower than 2.34 kPa measured in Test 3 (*H*=4 cm, *T*=1.8 s). Similar
371 conclusions can be also drawn for the cases with other wave heights. Fig. 9 illustrates
372 the effects of wave period on the maximum excess pore pressure at profile A-A with
373 the wave heights of *H*=4 cm and *H*=6 cm.
374
375 The results may be explained as follows. On one hand, the dynamic water pressure
376 and its gradient at the interface are related to wave period. The water pressure gradient
377 has great influence on the shear stress and the plastic strain (ε_p) in the silt bed. As
378 demonstrated in Kirca et al. (2013), the pore pressure builds up quickly at the node
379 and slowly at the anti-node for standing waves. Short period waves generally induce
380 weak oscillatory water pressure and small water pressure gradient at the interface. As
381 for long period waves, the oscillatory water pressure is large but the amplitude of
382 water pressure gradient is small at the interface. As such, the growth of the pore
383 pressure is negligible. On the other hand, the discharge volume of pore-water is
384 closely connected with wave period. When soil is compressed, the pore water cannot
385 be drained out timely for the case with short period waves. Therefore, the pore
386 pressure will accumulate during the wave loading. In contrary, the pore water has
387 sufficiently long time to drain out for the cases with relatively long period wave. Thus,
388 the residual pore pressure is negligible in such cases.
389
390 4.2.4 Soil response in the horizontal direction
391 Four time series of measured pore pressure at Point 4, Point 5, Point 7 and Point 8 in
392 Test 6 are shown in Fig. 10 to illustrate soil response along the direction of wave
393 propagation. The corresponding residual and oscillatory components are separated.

Fig. 10 demonstrates that soil is liquefied firstly at Point 4 (at the 9^{th} wave cycle, N=9), and at Point 5 ($N=13$), and then at Point 7 ($N=18$) and finally at Point 8 ($N=25$). This implies that the pore pressure builds up more rapidly at the upstream location. Moreover, the amplitude of oscillatory pore pressure attenuates along the direction of wave propagation (about 0.65 kPa at Point 4, 0.46 kPa at Point 5, 0.38 kPa at Point 7, and only 0.31 kPa at Point 8). According to the effects of wave height on soil response, the decrease of the amplitude of oscillatory pore pressure is justified.

However, the maximum residual pore pressures at these locations are almost identical. As to this phenomenon, the analysis of the experiments shows that the spherical stress (p) within the silt bed decreases along the direction of wave propagation. In addition, the plastic volumetric strain (ε_p) induced by the cyclic shear stress accumulates rapidly at upstream due to a relatively large wave height. Consequently, the excess pore pressure builds up rapidly at upstream and slowly at downstream. As pore pressure builds up rapidly at upstream, a pressure gradient is generated along the direction of wave propagation in the silt bed. This pressure gradient promotes the pore water spreading out along the direction of wave propagation and accelerates the pore pressure building up at the downstream.

4.3 Wave attenuation

Since soil response to wave loading will dissipate wave energy, different types of soil response, e.g., non-liquefaction response and liquefaction response, will result in different wave characteristics.

4.3.1 Wave attenuation in non-liquefaction situation

In Test 1, no soil liquefaction takes place and soil generally remains still. Wave

attenuation can be evaluated using the measured time series of water surface elevations $\eta(x,t)$, as shown in Fig. 11. According to the development of water surface elevation (Fig. 11(*a*)), the wave height, is estimated as 3.85 cm and almost remains the same over experimental duration (e.g. $\partial H(x,t)/\partial t = 0$). However, the pore pressure in silt bed has certain accumulation (see Fig. 11(*b*)-(*d*)).

For the spatial distribution of wave height, it damps slightly along the direction of wave propagation with the measured wave height from gauge 2 to gauge 6 being 4.01 cm, 3.92 cm, 3.85 cm, 3.78 cm, and 3.72 cm, respectively. The corresponding water surface records are shown in Fig. 12. Employing the linear fitting method, it is found that the wave-damping rate is about 0.0103.

It is well known that wave height is a reference parameter of wave energy. In non-liquefaction case, wave height almost remains the same at a fixed location. Due to the energy balance of water-soil system, wave attenuation does not change over time. In this situation, the wave height attenuates along the direction of wave propagation mainly due to bottom friction at the interface and percolation in the seabed. According to Yamamoto and Takahashi (1985), the wave height attenuation due to bottom friction and percolation can be expressed by

$$D_b = -\frac{8}{3\pi}\frac{k^2 f_w H_0}{\sinh kh(\sinh 2kh + 2kh)}, \quad D_p = -\frac{2k_s \omega k}{\nu(2kh + \sinh 2kh)} \tag{12}$$

where H_0 is the wave height at the entrance of the soil basin, D_b and D_p are the wave decay modulus induced by bottom friction and percolation, respectively. Due to these two factors, the wave height attenuates 0 cm, 0.0533 cm, 0.105 cm, 0.182 cm, 0.257 cm from gauge 2 to gauge 6, respectively, contributing over 90% to the total wave attenuation. The other parts of wave energy dissipation are due to the viscous friction

on the flume walls and the motion of the suspended soil particles. In the non-liquefaction case, the Coulomb friction loss between the soil particles is also inconspicuous because the relative displacement of soil particles is very small in silt bed. Consequently, the wave height almost has no obvious change at a fixed point, as those factors have little change over time.

4.3.2 Wave attenuation in liquefaction situation

Compared with the non-liquefaction case, wave in liquefied tests exhibits different features. Water surface elevation and excess pore pressure records at profile A-A in Test 8 and Test 14 are taken as examples to investigate wave response when soil liquefaction takes place. The results are shown in Fig. 13 in which top two are water surface elevations and the rests are excess pore pressure. It can be seen from the process of excess pore pressure that soil liquefaction depth is different in the two groups of tests. Under the condition of large wave, the liquefaction front moves downwards. The maximum liquefaction depth is found to be between 9 cm and 27 cm in Test 8 while it becomes larger than 27 cm in Test 14.

It can be found from the process of water surface elevation that the wave height experiences an attenuation period denoted by t_a at the beginning. After the attenuation process, the wave height tends to remain as a constant. The attenuation value of wave height is 1.62 cm in Test 8 and 1.7 cm in Test 14. Furthermore, the attenuation process is closely related to the liquefaction process. For convenience, the period from the start of waves loading to the soil liquefaction at a generic point *z* is denoted by $t_b(z)$ (the unit of *z* is cm). The experiments show that $t_b(z)$ increases with the soil depth d. In Test 8, the wave attenuation period t_a is slightly longer

than $t_b(\text{-}9)$. In Test 14, the result shows that t_a is also slightly longer than $t_b(\text{-}27)$. Similar results have been obtained for other liquefaction cases, suggesting that the wave attenuation period relates to the soil liquefaction progress.

Similar to wave change in non-liquefaction case, the attenuation of wave height in liquefaction case is enhanced along the direction of wave propagation. Moreover, the wave attenuation in liquefaction case is much larger than that in non-liquefaction case. For example, the wave height attenuates 50% in Test 2, resulting in 75% wave energy dissipated accordingly. However, this is based on our observations in the experiments, to the authors' best knowledge; there are no theoretical models for such a phenomenon available in the literature.

Fig. 14 is the five sets of the wave surface elevation records along the soil basin in Test 5. The final values of wave heights from gauge 2 to gauge 6 are 6.02 cm, 5.01 cm, 4.20 cm, 3.50 cm, and 3.20 cm, respectively. These measurements give the attenuation value, ΔH as -0.02 cm, 0.99 cm, 1.80 cm, 2.50 cm and 2.80 cm, respectively. This indicates that wave height damps greatly and very fast in liquefied silt bed. The wave height changes caused by bottom friction and percolation are calculated as 0.02 cm, 0.0825 cm, 0.150 cm, 0.234 cm, 0.303 cm. The damping due to these two parts only contributes 10% of the total wave attenuation; indicating that the bottom friction loss and the percolation loss are not the key attenuation factors in liquefied situation.

The above analysis is the result from individual case. To investigate the effects of wave height and period on the phenomenon of wave attenuation in general, Fig. 15 further presents the relation between the wave attenuation and wave height (Fig. 15(*a*)) and wave period (Fig. 15(*b*)). It is seen that both wave height and wave period have

significant effects on wave attenuation. Fig. 15(*a*) shows that the wave attenuates quickly in liquefaction cases and the attenuation grows when the wave height increases. Fig. 15(*b*) shows the effects of wave period on wave attenuation along the direction of wave propagation for the case of incident wave height 4 cm and 6 cm. Wave height changes induced by bottom friction and percolation are also displayed in the figures. In the tests with liquefaction, the wave height attenuation is larger for cases with shorter wave period. However, liquefaction depth in silt bed is deeper for the case with a longer wave period than that with a shorter wave period for the same incident wave height. In order to explain this phenomenon, the wave energy attenuation coefficient (*R*) is introduced.

Waves travelling across the soil bed have potential and kinetic energy and the time-averaged wave energy flux can be estimated as (Dean and Dalrymple, 1991)

$$P = \frac{1}{T}\int_{t}^{t+T}\int_{0}^{h+\eta} u\left(-\rho_w \frac{\partial \varphi}{\partial t}\right) dz dt \tag{13}$$

where φ is the velocity potential function of the wave. Under linear wave condition, the energy flux can be simplified as

$$P = \frac{1}{16}\rho_w g H^2 \frac{\omega}{k}\left(1+\frac{2kh}{\sinh 2kh}\right) \tag{14}$$

Differentiating *P* with respect to wave propagating distance x yields the wave energy attenuation coefficient, *R* (e.g. the period-averaged wave energy attenuation per unit time per unit crest length):

$$R = \frac{dP}{dx} = -\frac{\rho_w g \omega(\sinh 2kh + 2kh)}{16k \sinh 2kh}\frac{dH^2}{dx} \tag{15}$$

Fig. 16 shows the change of *R* along the direction of wave propagation for incident wave height of 4 cm and 6 cm, respectively. However, it should be noted that it is difficult to measure the wave height at all the position along the soil basin. Therefore,

520 the difference of wave heights measured by the adjacent wave gauges is used to
521 approximate the differential of midpoint.
522
523 The above results suggest that the wave energy attenuates more rapidly when soil
524 liquefaction occurs. This can be explained as follows. Firstly, comparing with the
525 non-liquefaction case, the rigidity of the liquefied silt bed is very small because of the
526 large residual pore pressure, and the shear strain and compressive strain become very
527 large. The relative displacement between the soil particles increases rapidly. Therefore,
528 the Coulomb friction loss in the silt bed with liquefaction increases dramatically.
529 Moreover, in the liquefied layer, the soil skeleton is eventual failure. As suggested by
530 Hwang et al. (2006), the liquefied soils can be treated as viscous fluid. In addition, the
531 kinematic viscosity of the loose silt is in the range of 0.01~0.1 m^2/s (Wen and Liu,
532 1998), which is 10^4~10^5 times larger than that of the pure water. Due to the large
533 viscosity in the liquefied layer, the thickness of the boundary layer is much larger than
534 the core region. Thus, the viscous damping in the liquefied layer is much larger than
535 that in the water layer and has significant effect on the wave motion.
536
537 4.3.3 Waveform evolution characteristics
538 The waveform evolutions measured by wave gauge 5 during Test 1, Test 5 and Test 9
539 are displayed in Fig. 17. The waveform has little change in non-liquefaction test (see
540 Fig. 17(a)). When the height of incident wave increases to 6 cm (e.g., Test 5), the
541 resulted wave height decreases and waveform becomes flat over time (see Fig. 17(b)).
542 Once the height of incident wave further increases to 8 cm (e.g., Test 9), the
543 waveform has shown nonlinear wave characteristics with sharp steep crest and flat
544 trough at the beginning. As the soil liquefied, wave energy and wave height decrease.
545 Furthermore, the measured waveform leans backward (as shown in Fig. 17(c)). This

suggests that the waveform leans forward along the direction of wave propagation due to the bottom friction.

5. Conclusions

A series of wave flume experiments are carried out to investigate the wave-induced liquefaction and corresponding wave attenuation in a silt bed. Water surface elevation, pore pressure accumulation and wave attenuation are measured simultaneously at several prescribed locations. The response features of excess pore pressure on vertical and horizontal profile are analyzed. The main conclusions from this study are:

(1) Soil liquefaction has significant effect on wave attenuation. Wave attenuation is weak in non-liquefaction situation. When liquefaction takes place, it becomes very large. Result shows that the damping rate in liquefaction case is over 10 times larger than that in the non-liquefaction situation.

(2)Due to wave attenuation in the horizontal direction, the amplitude of oscillatory pore pressure attenuates along the direction of wave propagation and the excess pore pressure builds up rapidly at upstream but slower at the downstream.

(3) Both the wave height and wave period have great effects on pore pressure response. Increase of the wave height increases the possibility of soil liquefaction. Liquefaction depth increases with the increase of wave period.

(4) The waveform has little change when the silt bed is not liquefied. However, noticeable waveform changes are obtained when soil liquefaction occurs.

Acknowledgements

The authors are grateful for the support by the National Natural Science Foundation of China (Grant No. 51479053), the 111 Project (Grant No. B12032), the marine renewable energy research project of State Oceanic Administration (GHME2015GC01), the Fundamental Research Funds for the Central University, China (Grant No. 2013B31614), the Colleges and Universities in Jiangsu Province Plans to Graduate Research and Innovation (Grant No. B1504708), and Open Foundation of State Key Laboratory of Hydrology-Water Resources and Hydraulic Engineering, Hohai University (Grant No: 2016491011). Comments and suggestions made by Reviewers have greatly improved the quality of the final manuscript.

578 **References**

579 Biot, M. A., 1941. General theory of three-dimensional consolidation. Journal of
580 Applied Physics 12(2), 155-164.

581 de Wit, P. J., Kranenburg, C., 1996. On the effects of a liquefied mud bed on wave and
582 flow characteristics. Journal of Hydraulic Research 34(1), 3-18.

583 Dean, R. G., Dalrymple, R. A., 1991. Water Wave Mechanics for Engineers and
584 Scientists, second edition. World Scientific, Singapore.

585 Foda, M. A., Tzang, S. Y., 1994. Resonant fluidization of silty soil by water waves.
586 Journal of Geophysical Research: Oceans (1978-2012) 99(C10), 20463-20475.

587 Gade H., 1958. Effects of a non-rigid impermeable bottom on plane surface waves in
588 shallow water, Journal of Marine Research 16, 61-82.

589 Hwang, J., Kim, C., Chung, C., Kim, M., 2006. Viscous fluid characteristics of
590 liquefied soils and behavior of piles subjected to flow of liquefied soils. Soil
591 Dynamics and Earthquake Engineering 26, 313-323.

592 Hsu, J., Jeng, D.-S., 1994. Wave-induced soil response in an unsaturated anisotropic
593 seabed of finite thickness. International Journal for Numerical and Analytical
594 Methods in Geomechanics, 18(11): 785–807.

595 Jeng, D.-S., Seymour, B. R., 2007. Simplified analytical approximation for pore-water
596 pressure buildup in marine sediments. Journal of Waterway Port Coastal and Ocean
597 Engineering, 133(4), 309-312.

598 Jeng, D.-S., Ou, J. 2010. 3D models for wave-induced pore pressures near breakwater
599 heads. Acta Mechanica, 215(1-4), 85-104.

600 Jeng, D.-S., Zhao, H. Y., 2015. Two-dimensional model for accumulation of pore
601 pressure in marine sediments. Journal of Waterway, Port, Coastal, and Ocean
602 Engineering 141(3), 04014042.

603 Jia, Y., Zhang, L., Zheng J., Liu X., Jeng D. S., Shan H., 2014. Effects of
604 wave-induced seabed liquefaction on sediment re-suspension in the Yellow River

605 Delta. Ocean Engineering 89(1), 146-156.
606 Kirca, V. O., Sumer, B. M., Fredsøe, J., 2013. Residual liquefaction of seabed under
607 standing waves. Journal of Waterway, Port, Coastal, and Ocean Engineering 139(6),
608 489-501.
609 Liao, C. C., Zhao, H. Y., Jeng D. S., 2015. Poro-Elasto-Plastic Model for the
610 Wave-Induced Liquefaction. Journal of Offshore Mechanics and Arctic Engineering
611 137(4), 1-8.
612 Lin, Z. B., Guo, Y. K., Jeng, D. S., Liao, C. C., Rey N., 2016. An integrated numerical
613 model for wave-soil-pipeline interactions. Coastal Engineering 108, 25-35.
614 Liu, B., Jeng, D. S., Ye, G. L., Yang, B., 2015. Laboratory study for pore pressures in
615 sandy deposit under wave loading. Ocean Engineering 106, 207-219.
616 Mathew, J., Baba, M., Kurian N. P., 1995. Mudbanks of the southwest coast of India. I:
617 Wave Characteristics. Journal of Coastal Research 11(1), 168-178.
618 Mathew, J., Baba, M., 1995. Mudbanks of the southwest coast of India. II: Wave-mud
619 interactions. Journal of Coastal Research 11(1), 179-187.
620 McDougal, W. G., Tsai, Y. T., Liu, P. L-F., Clukey, E. C., 1989. Wave-induced pore
621 water pressure accumulation in marine soils. Journal of Offshore Mechanics and
622 Arctic Engineering 111(1), 1-11.
623 Miyamoto, J., Sassa, S., Sekiguchi, H., 2004. Progressive solidification of a liquefied
624 sand layer during continued wave loading. Géotechnique 54(10), 617-629.
625 Sassa, S., Sekiguchi, H., 1999. Wave-induced liquefaction of beds of sand in a
626 centrifuge. Géotechnique 49(5), 621-638.
627 Sassa, S., Sekiguchi, H., 2001. Analysis of wave-induced liquefaction of sand beds.
628 Géotechnique 51(2), 115-126.
629 Seed, H. B., Rahman, M. S., 1978. Wave-induced pore pressure in relation to ocean
630 floor stability of cohesionless soils. Marine Geotechnology 3(2), 123-150.

631 Sekiguchi, H., Kita, K., Okamoto, O., 1995. Response of poro-elastoplastic beds to
632 standing waves. Soils and Foundations 35(3), 31-42.
633 Sui, T. T., Zhang, C., Guo, Y. K., Zheng, J. H., Jeng, D. S., Zhang, J. S., Zhang, W.,
634 2016.Three-dimensional numerical model for wave-induced seabed response
635 around mono-pile. Ships and Offshore Structures 11(6), 667-678.
636 Sumer, B.M., Dixen, F.H., Fredsøe, J., 2010. Cover stones on liquefiable soil bed
637 under waves. Coastal Engineering 57(9), 864-873.
638 Sumer, B.M., Fredsøe, J., 2002. The Mechanics of Scour in the Marine Environment.
639 World Scientific, Singapore.
640 Sumer, B. M., Hatipoglu, F., Fredsøe, J., Kaan Sumer, S., 2006. The sequence of
641 sediment behaviour during wave-induced liquefaction. Sedimentology 53(3),
642 611-629.
643 Tzang, S. Y., Ou, S. H., 2006. Laboratory flume studies on monochromatic wave-fine
644 sandy bed interactions: Part 1. Soil fluidization. Coastal Engineering 53(11),
645 965-982.
646 Tzang, S. Y., Ou, S. H., Hsu, T. W., 2009. Laboratory flume studies on
647 monochromatic wave-fine sandy bed interactions Part 2. Sediment suspensions.
648 Coastal Engineering 56(3), 230-243.
649 Tzang, S. Y., Chen, Y. L., Ou, S. H., 2011. Experimental investigations on
650 developments of velocity field near above a sandy bed during regular wave-induced
651 fluidized responses. Ocean Engineering 38(7), 868-877.
652 Wang, H., Liu, H. J., Zhang, M. S., 2014. Pore pressure response of seabed in
653 standing waves and its mechanism. Coastal Engineering 91, 213-219.
654 Wen, J., Liu, P.L.-F., 1998. Effects of seafloor conditions on water wave damping. In
655 Tyvand, P.A. (Ed.), Free-Surface Flows with Viscosity. Computational Mechanics
656 Publications.

Yamamoto, T. K., Koning, H. L., Sellmeijer, H., Hijum, E. V., 1978. On the response of a poro-elastic bed to water waves. Journal of Fluid Mechanics 87, 193-206.

Yamamoto, T., Takahashi, S., 1985. Wave damping by soil motion. Journal of Waterway, Port, Coastal and Ocean Engineering 111(1), 62-77.

Zen, K., Yamazaki, H., 1990. Oscillatory pore pressure and liquefaction in seabed induced by ocean waves. Soils and Foundations 30(4), 147-161.

Zhang, J. S., Jeng, D. S., Liu, P. L-F., 2011. Numerical study for waves propagating over a porous seabed around a submerged permeable breakwater: PORO-WSSI II model. Ocean Engineering 38(7), 954-966.

Zhang, J. S., Jeng, D. S., Liu, P. L-F., Zhang, C., 2012. Response of a porous seabed to water waves over permeable submerged breakwaters with Bragg reflection. Ocean Engineering 43(2), 1-12.

Zhang, J. S., Li, Q. Z., Ding, C., Zheng, J. H., Zhang, T. T., 2016. Experimental investigation of wave-driven pore-water pressure and wave attenuation in a sandy seabed. Advances in Mechanical Engineering 8(6), 1-10.

Table lists:

Figure captions in general

Fig. 14 Wave surface elevation records in Test 5: (a) gauge 2; (b) gauge 3; (c) gauge 4; (d) gauge 5; (e) gauge 6

Fig. 15 Effects of wave characteristics on wave attenuation (a) effects of wave height (b) effects of wave period

Fig. 16 Wave energy attenuation coefficient versus the length of wave propagated through silt bed

Fig. 17 Waveform evolution measured by wave gauge 5 (a): Test 1; (b): Test 5; (c): Test 9

Table 1

Parameter	Symbol	Value
Mean grain size	d_{50}	0.042 mm
Specific weight of sediment grains	γ_s	26.1 kN/m^3
Total specific weight of sediment	γ_t	19.8 kN/m^3
Maximum void ratio	e_{max}	1.10
Minimum void ratio	e_{min}	0.42
Void ratio	e	0.58
Relative density	D_r	0.76
Porosity	n	0.37
Coefficient of permeability	k_s	3.5×10^{-9} m/s
Submerged specific gravity	γ'	9.99 kN/m^3

708 Table 2

Test no.	H(cm)	T(sec)	t_w(sec)[1]	f_w	U_m(cm/s)	U_{fm}(cm/s)	R_e	θ	Response
1	4	1	340	0.0890	5.63	1.190	5.045×10^2	0.209	Non-liquefacti
2	4	1.4	455	0.0528	8.02	1.303	1.433×10^3	0.251	Liquefaction
3	4	1.8	345	0.0414	9.03	1.299	2.336×10^3	0.250	Liquefaction
4	5	1	450	0.0713	7.03	1.327	7.866×10^2	0.260	Liquefaction
5	6	1	400	0.0594	8.44	1.455	1.134×10^3	0.313	Liquefaction
6	6	1.4	425	0.0352	12.02	1.595	3.220×10^3	0.376	Liquefaction
7	6	1.8	415	0.0276	13.54	1.591	5.252×10^3	0.374	Liquefaction
8	7	1.4	425	0.0302	14.03	1.724	4.386×10^3	0.440	Liquefaction
9	8	1	400	0.0445	11.26	1.680	2.018×10^3	0.417	Liquefaction
10	8	1.4	360	0.0264	16.03	1.842	5.726×10^3	0.502	Liquefaction
11	8	1.8	310	0.0207	18.06	1.837	9.344×10^3	0.499	Liquefaction
12	9	1.4	330	0.0235	18.04	1.956	7.251×10^3	0.566	Liquefaction
13	10	1	352	0.0356	14.07	1.877	3.151×10^3	0.521	Liquefaction
14	10	1.4	330	0.0211	20.04	2.058	8.948×10^3	0.626	Liquefaction
15	10	1.8	362	0.0166	22.57	2.056	1.459×10^4	0.625	Liquefaction

709 ([1]Abbreviations are t_w, duration of wave loading)

710

711

712

713

714 Fig. 1

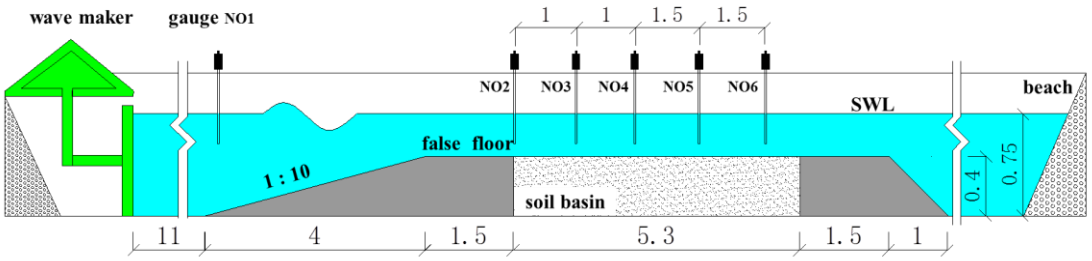

715

716 (*a*)

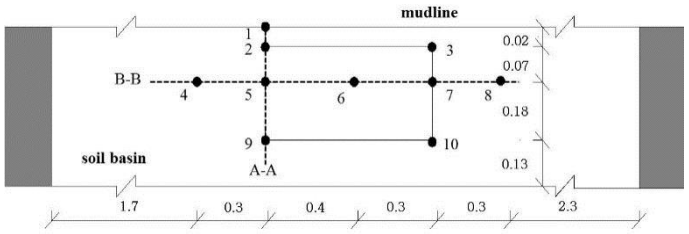

717

718 (*b*)

719

720

721 Fig. 2

722

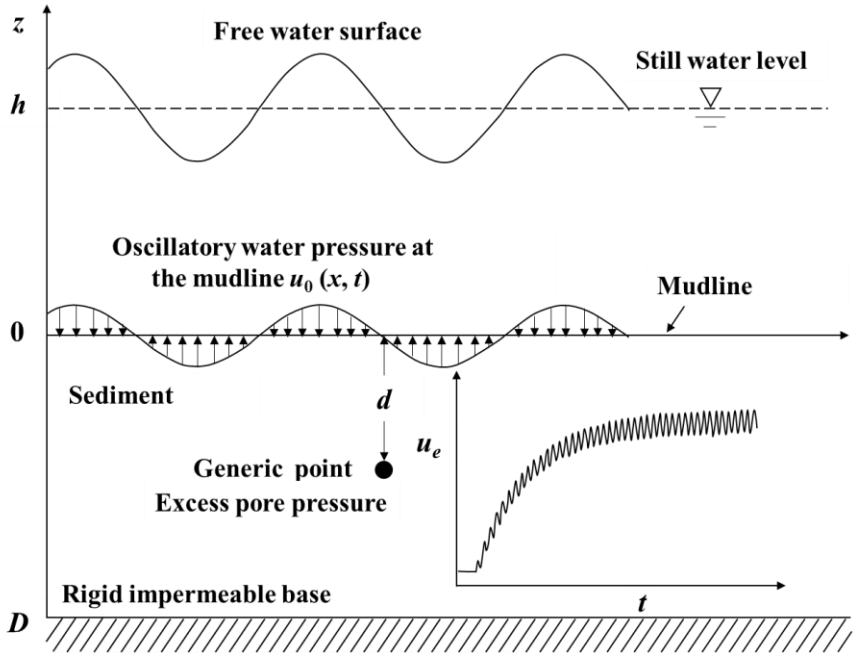

723

724

725

Fig. 3

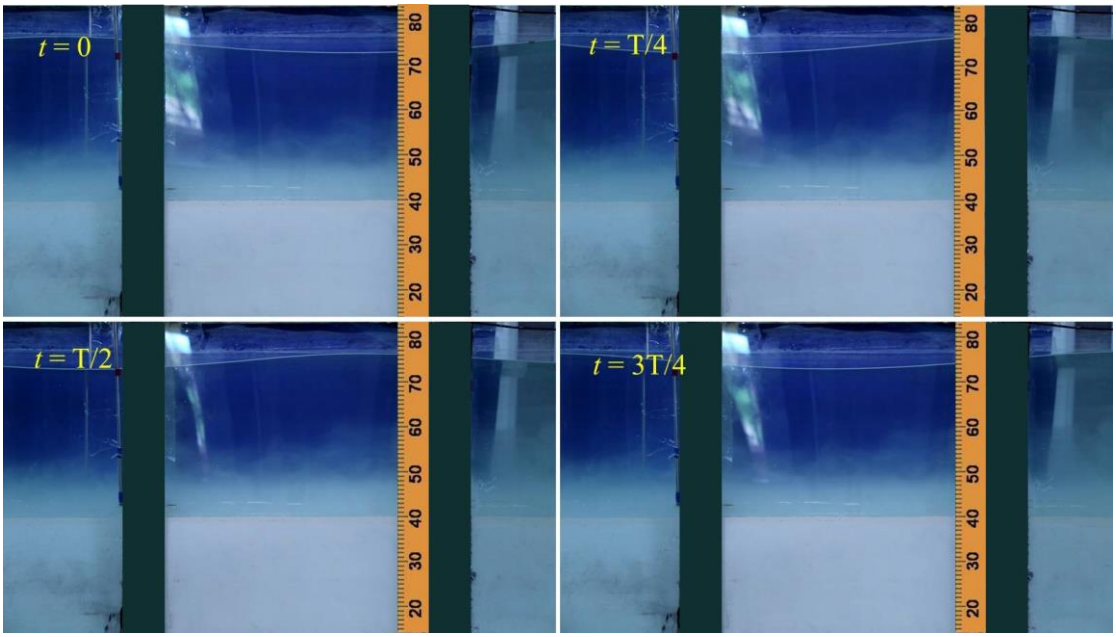

(*a*)

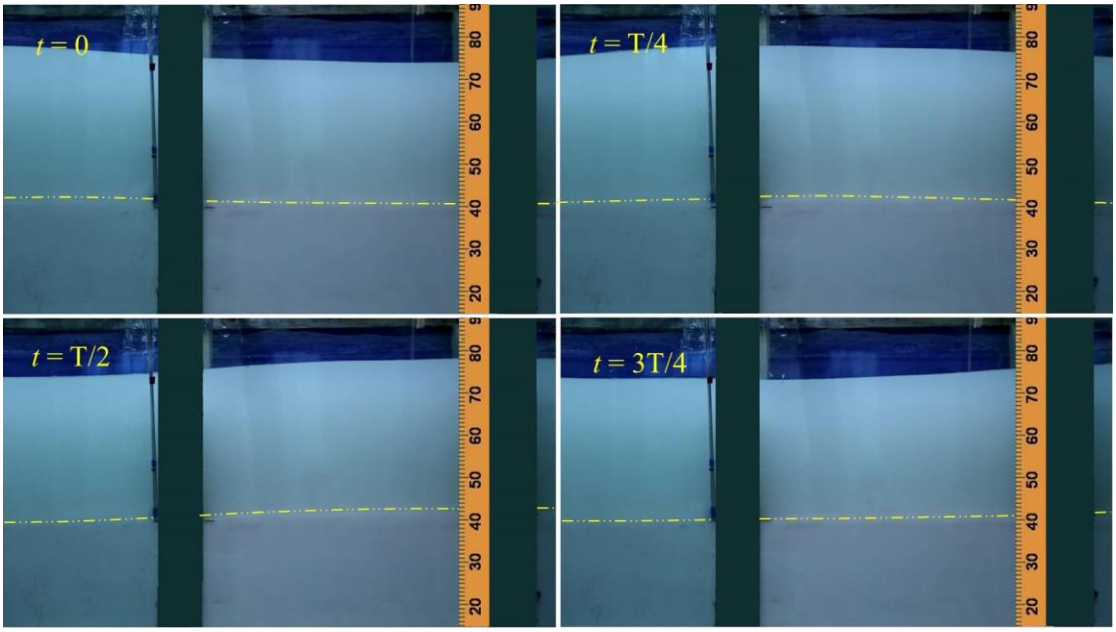

(*b*)

734

735 Fig. 4

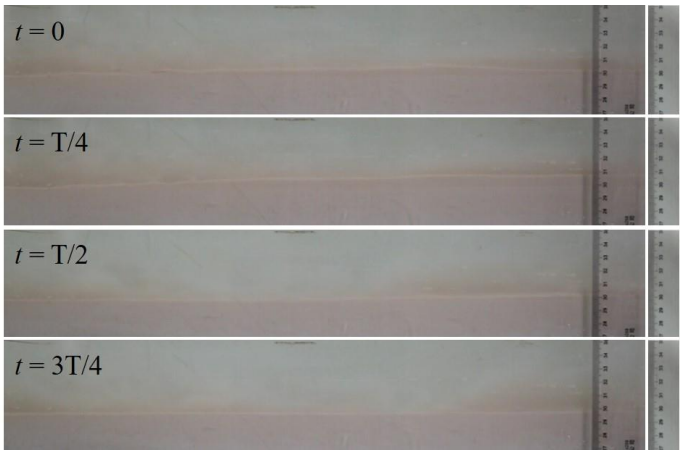

736

737

Fig. 5

(*a*)

(*b*)

745

746 Fig. 6

747

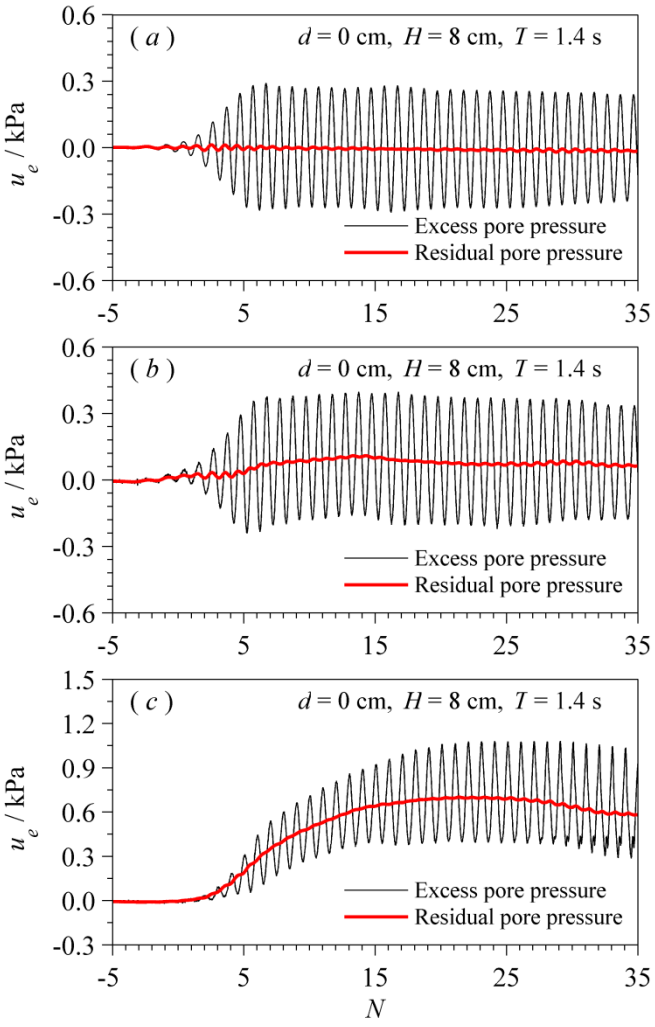

748

749

750

751

752 Fig. 7

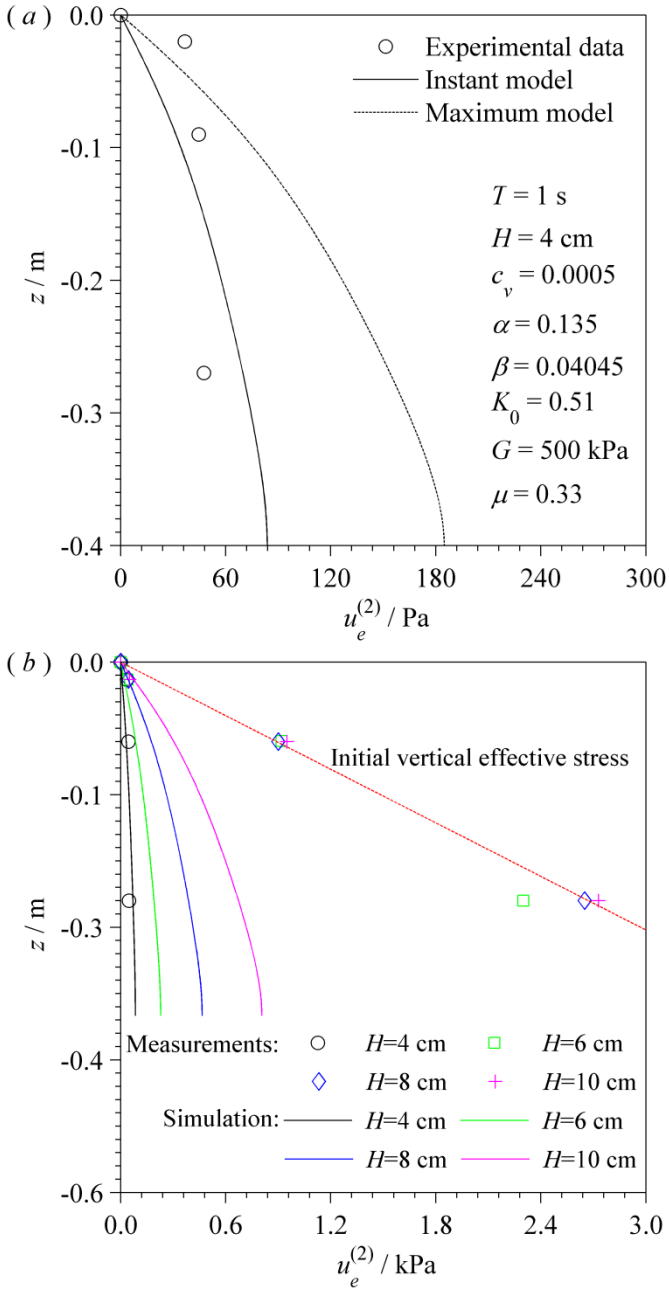

753

754

755

756 Fig. 8

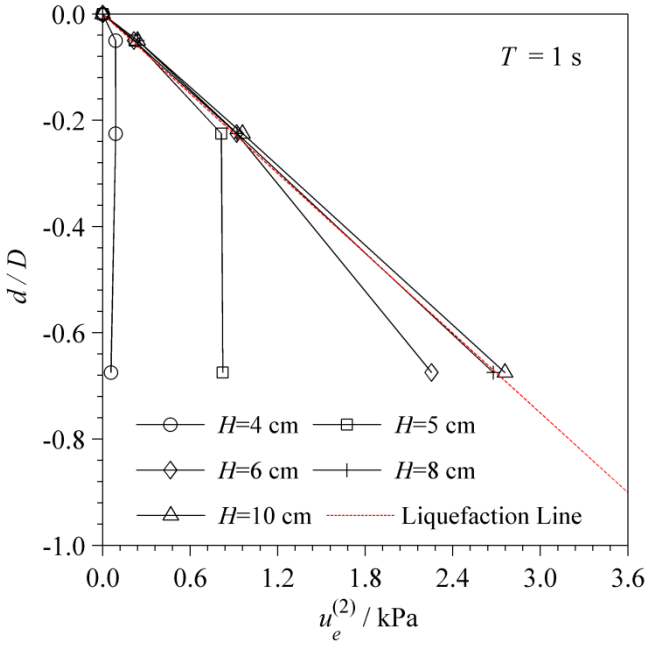

757

758

759

760 Fig. 9

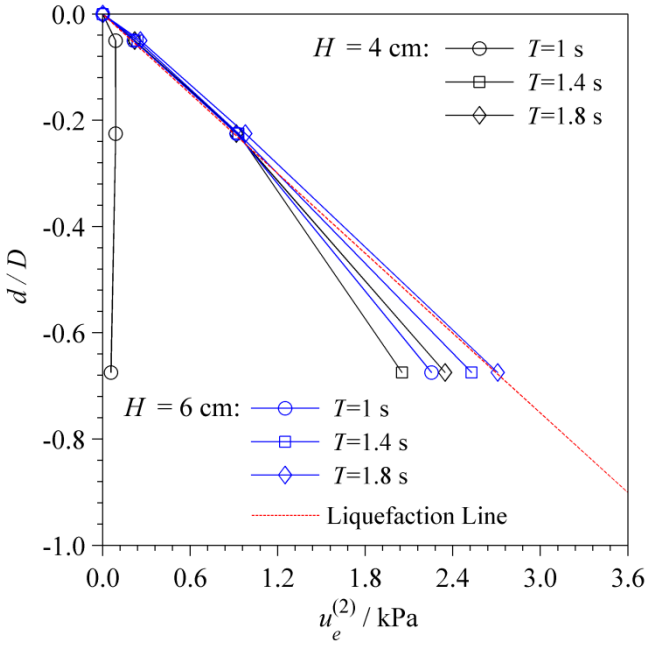

761

762

763

764 Fig. 10

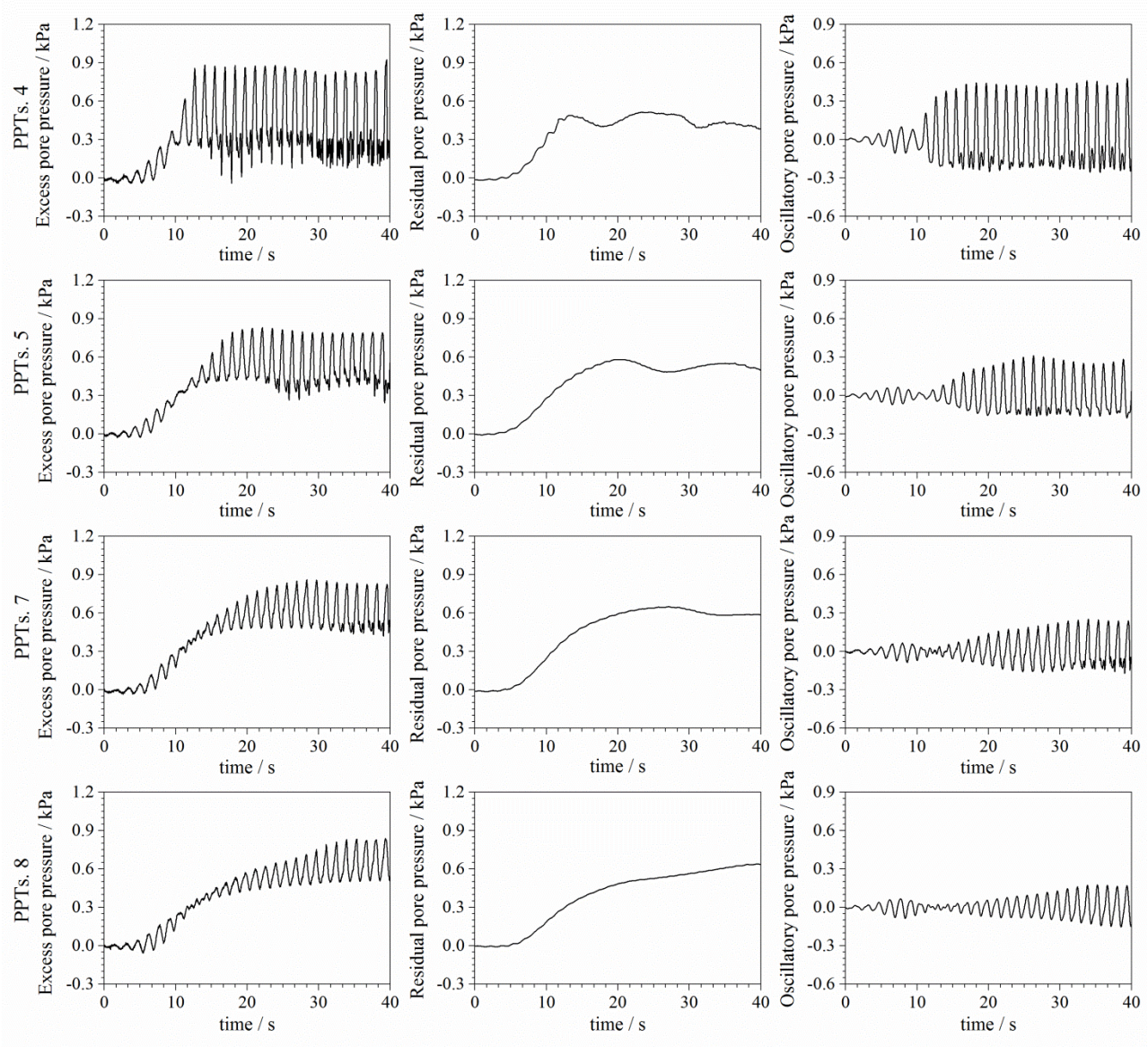

765

766

767

768 Fig. 11

769

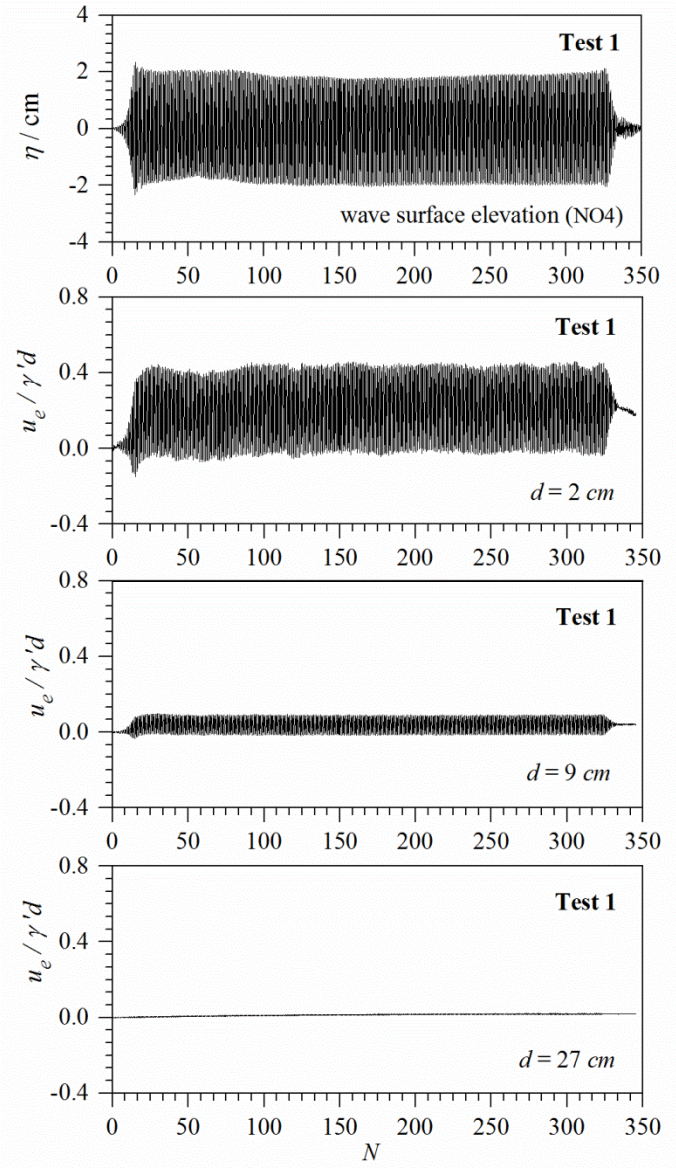

770

771

772

773 Fig. 12

774

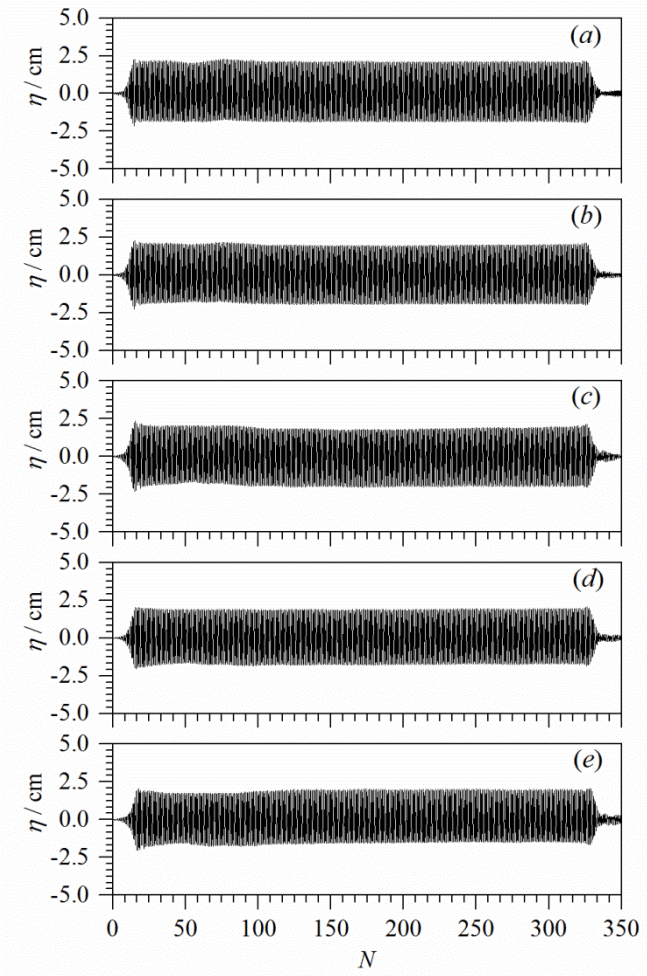

775

776

777

778 Fig. 13

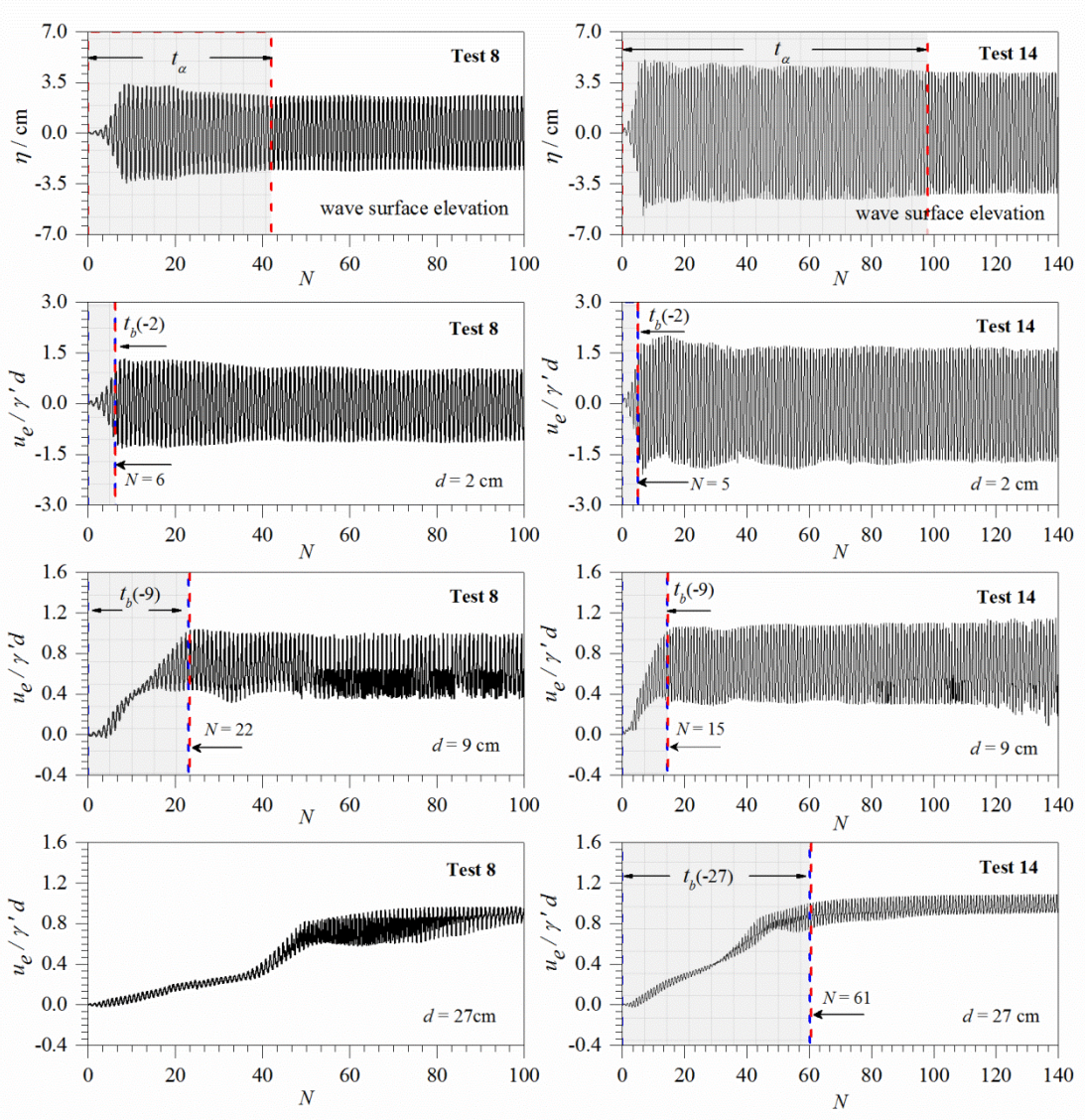

779

780

781

782

783 Fig. 14

784

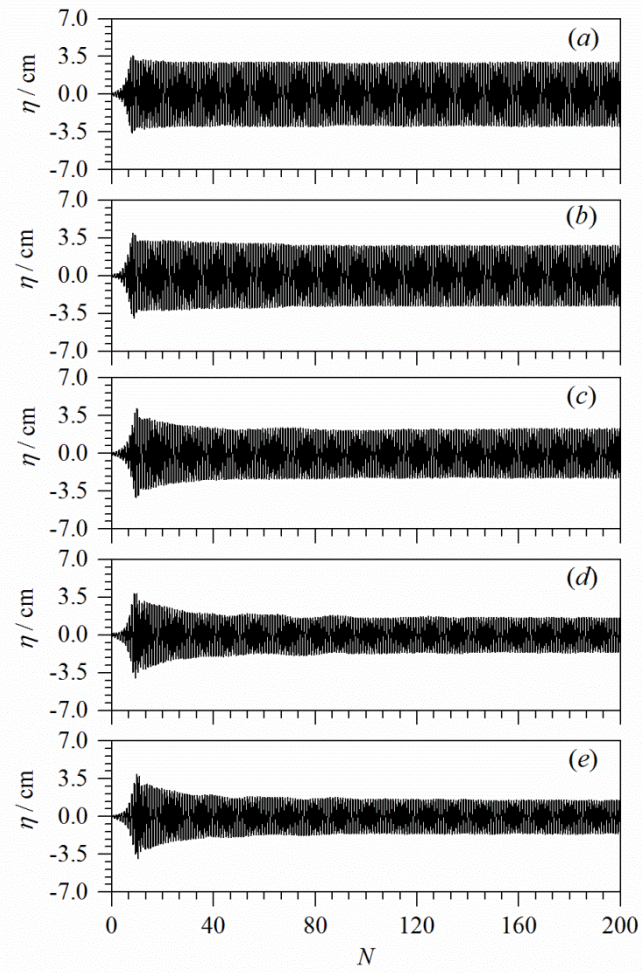

785

786

787

788 Fig. 15.tif

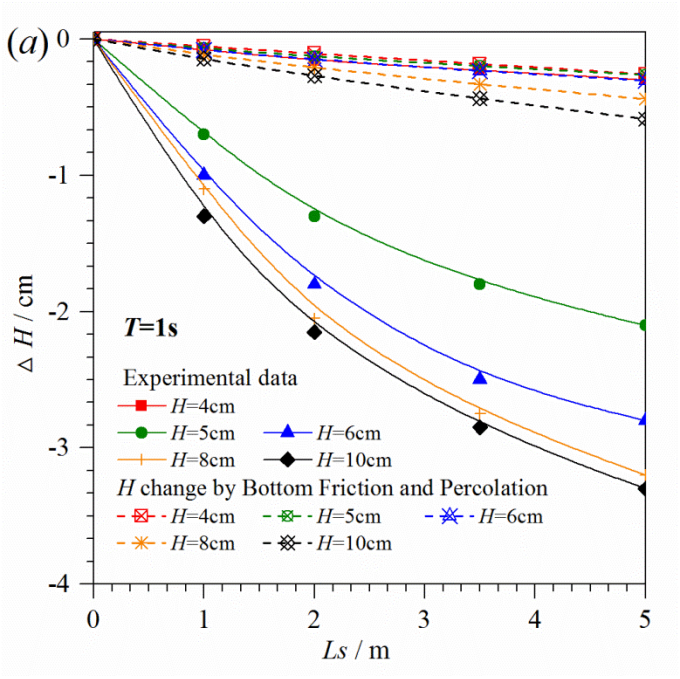

789

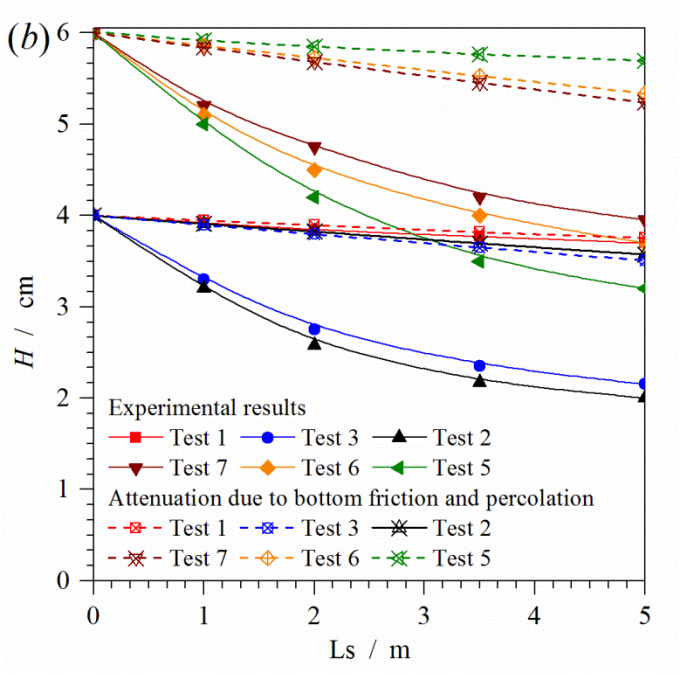

790

791

792

793 Fig. 16

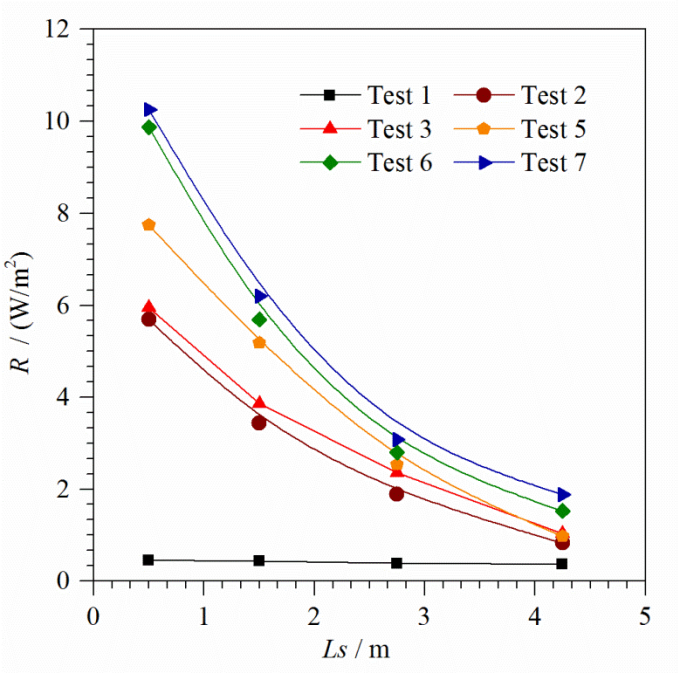

794

795

796

797 Fig. 17

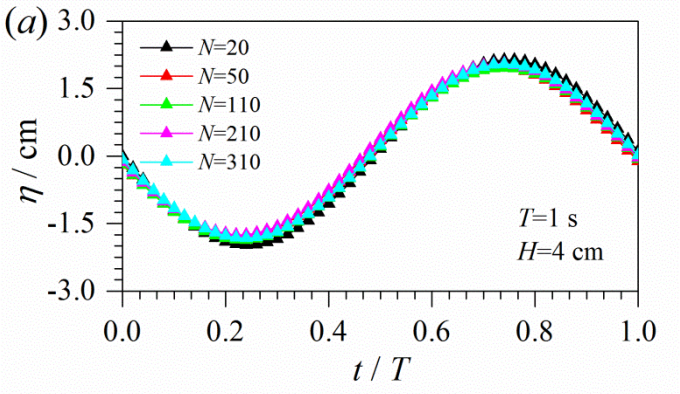

798

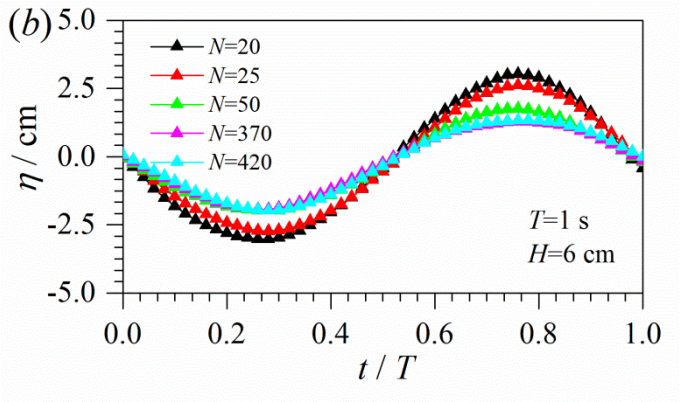

799

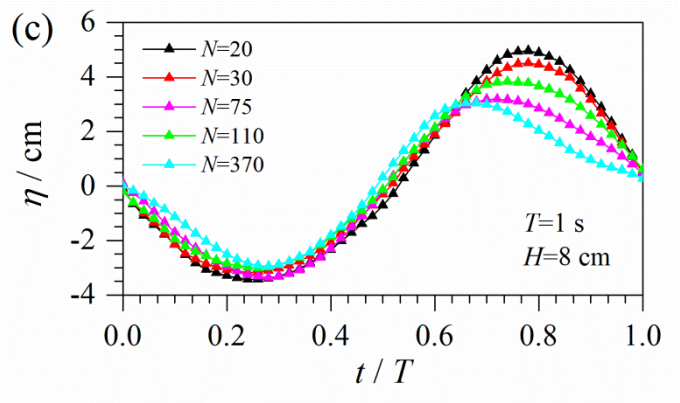

800

801

802

803

804